



New flexible CsPbBr₃-based scintillator for X-ray tomography

Zhi-Wei Lü¹ · Gong-Xiang Wei¹ · Han-Qiu Wang¹ · Yu Guan¹ · Ning Jiang¹ · Yun-Yan Liu¹ · Zhao Li¹ · Hua Qin¹ · Hui-Qiang Liu¹

Received: 13 April 2022 / Revised: 14 June 2022 / Accepted: 20 June 2022 / Published online: 12 August 2022

© The Author(s), under exclusive licence to China Science Publishing & Media Ltd. (Science Press), Shanghai Institute of Applied Physics, the Chinese Academy of Sciences, Chinese Nuclear Society 2022

Abstract The evolution of lead halide perovskites used for X-ray imaging scintillators has been facilitated by the development of solution-processable semiconductors characterized by large-area, flexible, fast photoresponse. The stability and durability of these new perovskites are insufficient to achieve extended computed tomography scanning times with hard X-rays. In this study, we fabricated a self-assembled CsPbBr₃-based scintillator film with a flexible large-area uniform thickness using a new room-temperature solution-processable method. The sensitivity and responsivity of X-ray photon conversion were quantitatively measured and showed a good linear response relationship suitable for X-ray imaging. We also demonstrated, for the first time, that the self-assembled CsPbBr₃-based scintillator has good stability for hard X-ray microtomography. Therefore, such an inexpensive solution-processed semiconductor easily prepared at room temperature can be used as a hard X-ray scintillator and equipped with flexible CsPbBr₃-based X-ray detectors. It has great potential in three-dimensional high-resolution phase-contrast X-ray-imaging applications in biomedicine and material science because of its heavy Pb and Br atoms.

Keywords X-ray scintillator · X-ray illumination · Computed tomography · CsPbBr₃-based film perovskite · Solution-processable semiconductor

1 Introduction

Since the discovery of X-rays, X-ray imaging techniques have rapidly advanced and are widely used for nondestructive detection in many fields, such as biomedicine, material science, and industrial production [1–4]. With the emergence of new optoelectronic devices, X-ray detectors coupled with various scintillators have improved X-ray imaging and tomography [5]. Many X-ray scintillators that can effectively convert X-rays into visible light have been made from CsI:Tl, P₄₃-Gd₂O₂S:Tb, Y₃Al₅O₁₂:Ce⁺, and Bi₃Ge₄O₁₂ crystals with varying thicknesses [6–8]. Almost all these scintillators are inflexible bulk crystals or powders grown using the Czochralski method at temperatures exceeding 1700 °C with complex processing and synthesis procedures [9]. In addition, plastic scintillators with a simple preparation process and stable performance are typically used for the intensity detection of cosmic rays, γ -rays, and neutrino [10–13].

With the development of organic and inorganic semiconductors, new X-ray photon scintillators have been widely used to improve conventional X-ray imaging. Solution-processed organic and inorganic semiconductors have attracted considerable attention in the last decade. X-ray scintillators made from solution-processed organic semiconductors are characterized by controllable thickness, short scintillation decay time (typically 1–30 ns), and good usability owing to their simple preparation process [14–16]. Most of them are produced from toxic solutions,

Zhi-Wei Lü and Gong-Xiang Wei have equally contributed to their work.

✉ Hui-Qiang Liu
liuhq@sdut.edu.cn

Hua Qin
zfqinh@163.com

¹ School of Physics and Optoelectronic Engineering, Shandong University of Technology, Zibo 255000, China

such as $C_{18}H_{14}$, $C_{20}H_{14}N_2O$, and $C_{15}H_{11}NO$, and are susceptible to photobleaching and oxygen quenching, which hampers their practical applications in many fields [17–20]. The conversion efficiency of organic scintillators scaled with atomic number is significantly low because of their weak X-ray absorption. In addition, single-crystal CsI:Tl scintillators are widely used for X-ray scintillators because of their ultrahigh photoluminescence yield (PLQY) and prolonged afterglow. Optimization is possible by codoping various aliovalent ions, such as Yb co-doped CsI:Tl crystals suppressed afterglow down to 80 ms [21]. For single-crystal $Y_3Al_5O_{12}$, the typical photoluminescence (PL) lifetimes are within 8–80 ns, and the PLQY of optimized $Y_3Al_5O_{12}:Ce$ approaches 60,000 photon MeV^{-1} with an emission wavelength of 550 nm, facilitating coupling with silicon photodiodes and charge-coupled device detectors [22]. However, its slow crystal growth and complicated synthesis process result in high costs. Because of its high density (7.34 g/cm^3), wide bandgap (4.6 eV), and high radiation resistance, the powder phosphor screen of $Gd_2O_2S:Tb^+$ has also been applied to X-ray imaging screens, despite the loss of resolution caused by powder scattering [23].

Recently, solution-processed lead halide perovskites (SLHPs) have attracted significant attention owing to their tunable bandgap, wide absorption spectrum, and high photon conversion efficiency in detecting X-ray photons, with potential applications in X-ray imaging devices [24, 25]. Despite the excellent performance of SLHP nanocells (NCs) in solutions, the PLQY decreases by approximately 30% from NC solutions to films because of the subsequent loss of surface passivation, leading to poor stability and a limited film area [26, 27]. Based on light-matter interactions, many SLHP nanoplatelets can be transformed into bulk analogs via continuous laser irradiation [28]. A single SLHP film exhibits hybrid perovskite single crystals with heterogeneous substrates, with a small valid area of 5.8–10 mm^2 [29, 30]. In particular, the lead-halide perovskite ($MAPbI_3$) characterized with organic–inorganic hybrid perovskite has attracted considerable research interest because of its excellent properties in photovoltaic and optoelectronic devices. However, the disadvantage of organic–inorganic perovskites is their environmental instability, which limits their application in photoelectronic imaging devices. Currently, all inorganic $CsPbX_3$ ($X = Br, Cl, \text{ and } I$) perovskites have become the focus of studying new perovskite materials because of their environmental stability, excellent photoelectronic characteristics, and low trap density. They have already been used in various photodetectors and diode devices. Studies have shown that the morphology of $CsPbX_3$ perovskite nanostructures can be controlled precisely, and different units of $CsPbX_3$ perovskite, including nanodots, nanowires, and

nanosheets, have been successfully developed [31–35]. For two-dimensional (2D) nanosheets, the $CsPbX_3$ perovskite can be an excellent alternative material for X-ray imaging because of its advantages, such as few grain boundaries and defects, high formation energy, improved lateral electrical transmission characteristics, and reduced optical exciton quenching [36].

In this study, we synthesized a high-quality flexible SLHP film for X-ray scintillators with controllable thickness and uniformity, self-assembled from solutions of $CsPbBr_3$ nanosheets at room temperature (25 °C). This film exhibited advantages for X-ray imaging, such as controllable thickness, uniform and large crack-free area, high light yield, and a linear X-ray photon response. The excellent imaging performance with a $CsPbBr_3$ film-based X-ray scintillator was first demonstrated based on our tomographic data with a high resolution (SR) and contrast-to-noise ratio (CNR) using biological samples. The self-assembled $CsPbBr_3$ nanosheets also exhibited good stability in tomographic imaging with extremely high-flux synchrotron radiation X-ray beams. Our experimental results demonstrate that the new self-assembled $CsPbBr_3$ -based X-ray scintillator is an alternative X-ray scintillator with a high resolution and large field of view, with the potential for applications in high-precision full-field radiography and tomography for large samples.

2 Materials and methods

2.1 Solution-processed flexible $CsPbBr_3$ -based X-ray scintillator

The relevant chemical reagents used to prepare flexible $CsPbBr_3$ films were purchased as follows: CsAc with a trace metal basis (99.9%), $PbBr_2$ (99.9%), OcAm (99.0%), OcAc (99.0%), and PrOH (99.0%) from Macklin Chemical Co., Ltd. (Shanghai, China); hexane (99.5%) and toluene (99.5%) from Aladdin Chemical Co., Ltd. (Shanghai, China). All the chemical reagents were not purified further. The processing flowchart is shown in Fig. 1.

2.2 X-ray imaging measurements

X-ray irradiation of the flexible $CsPbBr_3$ film was performed to measure its fluorescence efficiency, linear dynamic range, and spectral characteristics using a microfocus X-ray tube (25 W, XWT-160-THE, Germany) with adjustable tube voltages and currents of 20–160 kV and 50–600 μA , respectively, as shown in Fig. 2a and b. The source-to-sample distance was varied within the range of 30–500 mm, which is suitable for most imaging requirements. An X-ray radiation dosimeter (821021-A,

Fig. 1 Flowchart of CsPbBr₃ film preparation

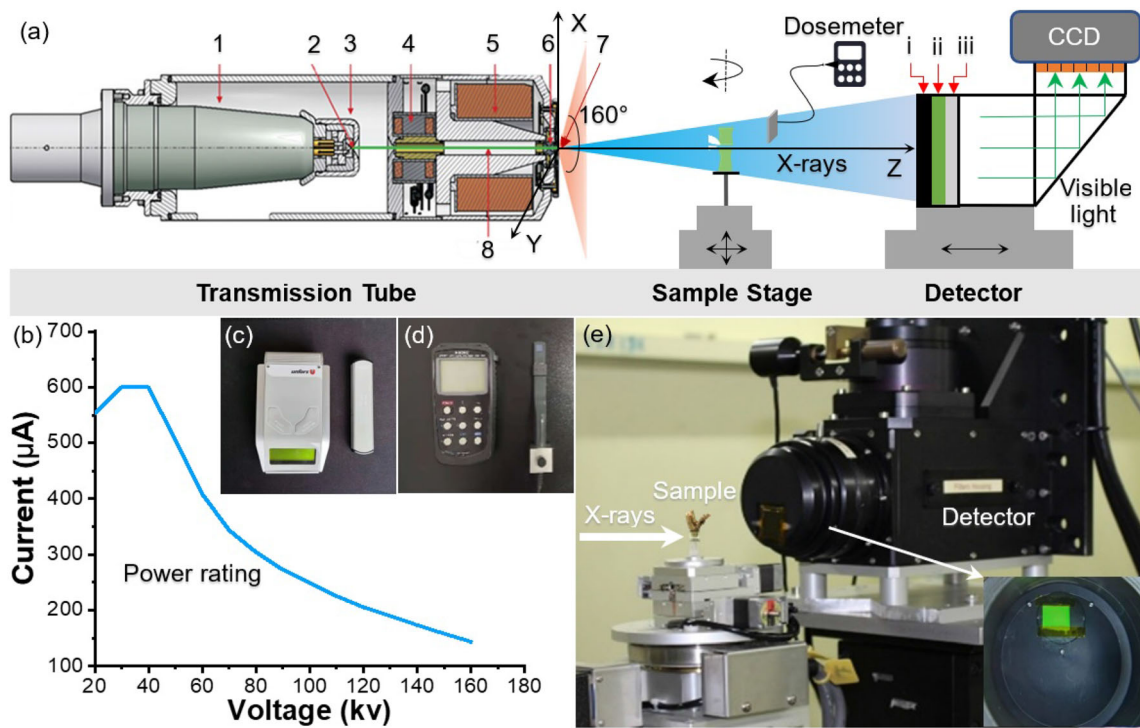
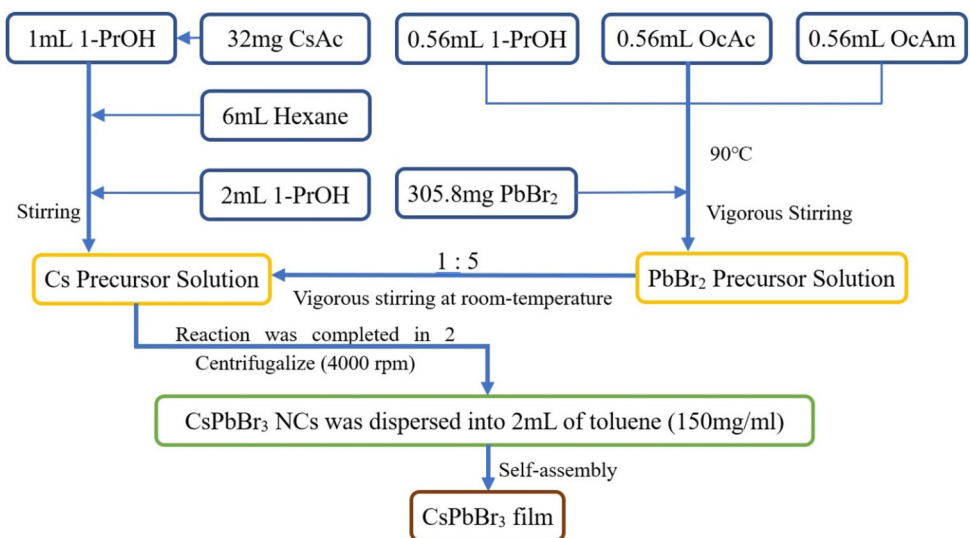


Fig. 2 (Color online) Description of experimental platform and main equipment parameter testing. **a** Schematic of X-ray imaging system with CsPbBr₃-based scintillator and measurement of X-ray photons and visible light conversion efficiency of CsPbBr₃ film, including transmission tube. Three-axis precision sample stage and new perovskite detector. 1 HT-Receptacle, 2 Electron emitter, 3 Grid

cap, 4 Deflection unit, 5 Focusing coil, 6 Objective aperture, 7 Transmission target, 8 Electron beam, i Carbon glass, ii CsPbBr₃ film, iii PET substrate. **b** Voltage and current characteristics of X-ray tube. **c** Dosimeter. **d** Optical power meter. **e** X-ray detector with CsPbBr₃ film fixed on internal surface of lens cap as scintillator for imaging

UNFORS, Sweden) was used to calibrate the dose rate intensity distribution in the X-ray field, and an optical power meter (3664, HIOKI, Japan) was placed on the back surface of the samples to measure the intensity of the visible light converted by our CsPbBr₃ film, as shown in Fig. 2d. Subsequently, its radioluminescence (RL)

performance was determined by calculating the conversion ratio. The tomographic measurements of a strongly absorbing object (cable head) and a weakly absorbing object (bamboo) were performed using an X-ray detector (C11440-22C, Hamamatsu, Japan) equipped with a 20-μm-thick CsPbBr₃-based scintillator and lens assembly via

synchrotron phase-contrast imaging at BL13HB@SSRF, as shown in Fig. 2e. A phase-retrieval algorithm was employed to obtain high-phase-contrast three-dimensional (3D) images, facilitating the discovery of tiny structural features of biological samples. The experimental conditions were as follows: photon energy = 15 keV; photon flux = 3.0×10^{11} phs/s/mm²; effective pixel size = 3.25 μ m; exposure time = 4000 ms; sample-to-detector dimension = 80 mm; projections = 1080; total scanning time = 90 min.

2.3 Image analysis

To quantitatively analyze the imaging performance of the CsPbBr₃-based scintillator, we calculated the CNR and SR of the radiographic and tomographic images. For the CNR calculations, Eq. (1) is used:

$$\text{CNR} = 2 \frac{|S_{\text{obj}} - S_{\text{bg}}|}{\sqrt{\sigma_{\text{obj}}^2 + \sigma_{\text{bg}}^2}}, \quad (1)$$

where S and σ are the mean and standard deviation of the pixel value of a homogeneous region, respectively, obj and bg denote the object and background regions of interest (ROIs), respectively, manually defined in Fig. 5a–c.

Both resolution criteria were employed to calculate radiographic and tomographic SRs to comprehensively reveal the fine structure resolution. One resolution was estimated from the full-width at half-maximum (FWHM) of the line spread function (LSF) curves derived from the step response function fitted with an error function by the average of a least-squares fit [37]. The other was determined using a criterion based on Fourier analysis with the profile lines of the object and by calculating its power spectral density (PSD). The convergence value of the PSD was considered the noise baseline for the images. According to Shannon's theorem, the corresponding spatial frequency (SF) can be determined using twice the PSD value of the noise baseline. The SR, X_{res} , is calculated as follows:

$$X_{\text{res}} = p_{\text{size}} \left(\frac{x_n}{k_{\text{res}}} \right), \quad (2)$$

where X_{res} is the pixel size of the detector, x_n is the number of pixels for the line profile, and k_{res} is the SF.

3 Results

3.1 X-ray PL of CsPbBr₃ film

The large-area CsPbBr₃ thin film was synthesized using a room-temperature coprecipitation technique and the self-assembly process shown in Fig. 1. It was uniform and

crack-free without any encapsulation under ambient light (Fig. 3a); it had an area of 1575 mm² (45 mm \times 35 mm) and could be readily cast into larger area films with the required thicknesses for X-ray imaging applications. Additionally, the CsPbBr₃ film used for the scintillators was formed via a self-assembly process, and the thickness was controlled by dropping a specific amount of CsPbBr₃ colloid on a flat substrate, with good smoothness measured using scanning electron microscopy (SEM). Moreover, the film exhibited bright green PL excited by the X-ray beams, as shown in Fig. 3b, directly revealing the coexistence of multiple quantum wells with a high PLQY. Thus, it can be used as a warning sign for ionizing radiation, as shown in Fig. 3c, which is made of a CsPbBr₃ thin film and hollow black cardboard and placed in an X-ray field. Moreover, the photoluminescence of this flexible CsPbBr₃ film with different curvatures as a bending cycle (Fig. 3d) exhibited stable photoluminescence properties under repeated bending cycles for over 1000 times without physical damage, indicating remarkable flexibility. The X-ray diffraction (XRD) spectra of the CsPbBr₃ film suggested seven characteristic peaks at 15.18°, 21.55°, 26.48°, 30.64°, 34.37°, 37.76°, and 43.89°, corresponding to the crystalline phases of 100, 110, 111, 200, 210, 211, and 220 (JCPDS PDF # 54-0752), as shown in Fig. 3e. This demonstrates the superstructural features of the film. The micromorphology of the CsPbBr₃ film with a thickness of 28 μ m was measured using SEM from the top over a large area (700 μ m \times 500 μ m), as shown in Fig. 3f, and was relatively flat without any cracks. The magnified inset shows a smooth, micropore-free surface. The PL spectra were measured using an emission spectrometer (PG2000 Pro, Idea Optics) with 400 nm excitation and a center wavelength of 522 nm (Fig. 3g), which matched the maximum wavelength response of a complementary metal–oxide–semiconductor sensor. Additionally, within the range of the human-eye sensitive-light wavelength, fluorescent signage was achieved (Fig. 3c). Figure 3h shows the PL decay trace at 520 nm, indicating a lifetime of 11.5 ns, which is far shorter than that of NaI:TI (\sim 200 ns). The RL efficiency, which is related to the X-ray attenuation length of the perovskite film, was determined (Fig. 3i). The RL intensity increased with increasing film thickness within the range of 5–80 μ m, and a saturated value of the RL intensity was reached when the thickness was 28 μ m. This suggests that the optimal film thickness can be achieved. In addition, a single-crystal scintillator made of cerium-dropped lutetium-aluminum garnet (Ce:LuAG) also attained a similar PL peak position, located at 520 nm. However, the light yield of the CsPbBr₃ perovskite film was approximately 21,000 photons/MeV, which is higher than the \sim 18,000 photons/MeV of a commercial Ce:LuAG single-crystal scintillator.

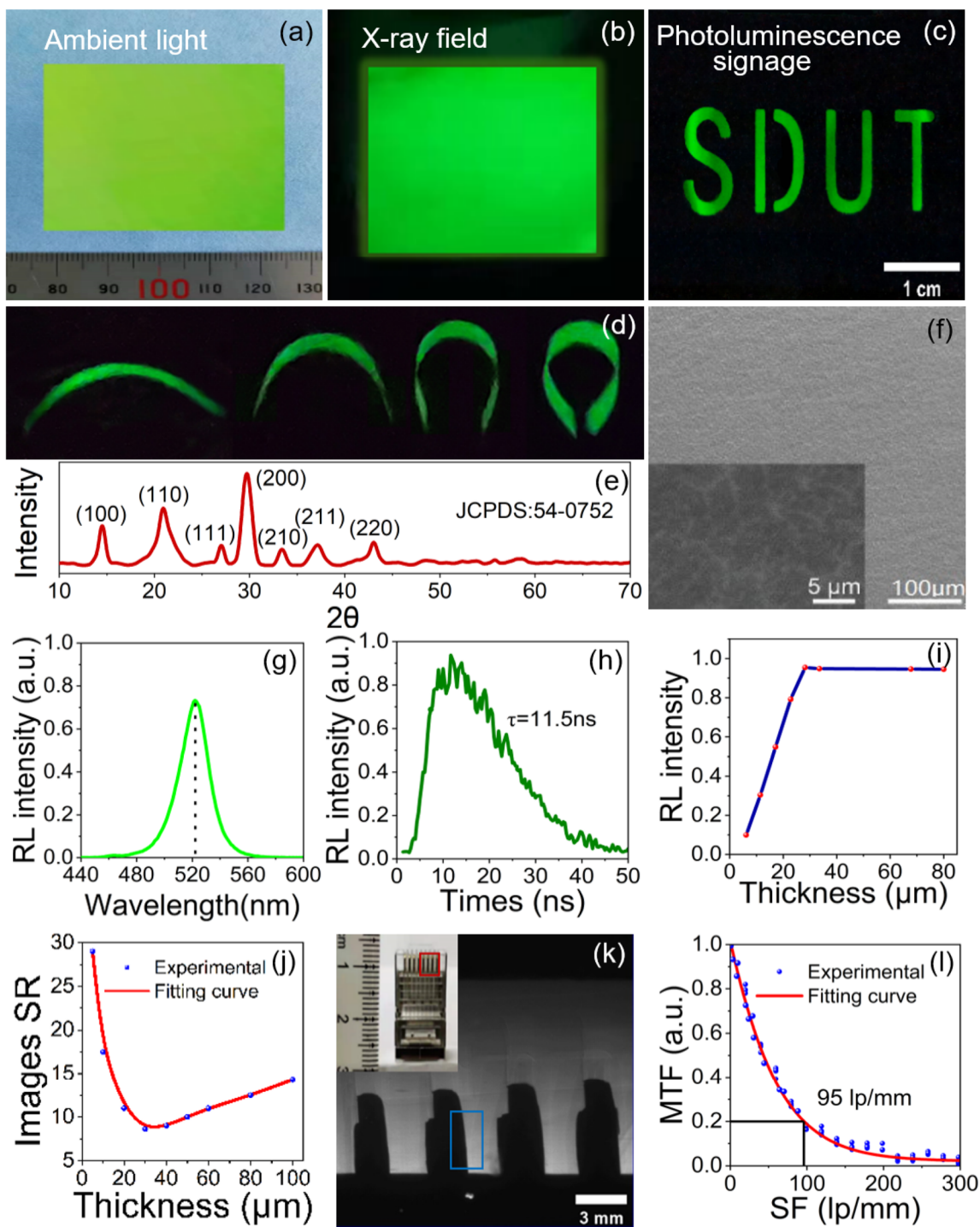


Fig. 3 (Color online) Scintillating film self-assembled from CsPbBr₃ nanosheets. **a** Digital photograph of CsPbBr₃ scintillator on polymer film with 45 mm × 35 mm under normal lighting. **b** Fluorescent photograph of **(a)** excited by X-ray of 60 kV. **c** Fluorescent signage of SDUT illuminated by X-ray beams. **d** Photoluminescence images of CsPbBr₃ film in different curvatures. **e** XRD pattern of CsPbBr₃ film showing seven significant peaks. **f** SEM image showing flatness of thin film. **g** PL spectrum of CsPbBr₃ scintillating film excited by

ultraviolet of 400 nm. **h** CsPbBr₃-based scintillator decay time of $\tau = 11.5$ ns. **i** Thickness dependence of RL intensity showing an optimal value at 28 μm . **j** Sensitivity of different film thicknesses showing optimal thickness at 28 μm . **k** Radiographic image of cable head (inset); the blue rectangle used for modulation transfer function (MTF) calculations of slanted edge. **l** MTF of X-ray radiography using CsPbBr₃ scintillating film

The SRs of the CsPbBr₃ films with different thicknesses (5–100 μm) were measured and fitted (Fig. 3j). The SR increased and then decreased with increasing thickness, reaching 8.6 μm at a thickness of 30 μm with an optimal SNR. Good sensitivity was achieved through the trade-off between photoluminescence efficiency and SR. By assembling the CsPbBr₃ film with an X-ray detector as a scintillator, the radiographic image of the test sample (a cable head with a height of approximately 20 mm) could be obtained with the display of inner microstructures and showed an excellent imaging capacity (Fig. 3k). The sharp edges of the absorption contrast were generated by density differences between different components and were effectively used as slanted edges to estimate the modulation transfer function of the testing sample (Fig. 3l). The SR of CsPbBr₃-based scintillators can reach up to 95 lp/mm.

3.2 Characterization of sensitivity and conversion

Based on the RL effect of the CsPbBr₃ film induced by X-rays, the sensitivity and conversion characteristics were measured 10 times using our laboratory X-ray source over three months (Fig. 4). Figure 4a and d shows the proportional relationships between the X-ray dose rate and the varying tube currents and voltages, respectively, at different propagation distances. Accurate distribution of the radiation dose in the cone X-ray field was observed, from the Gaussian distribution to the uniform field shown in Fig. 4g–i, facilitating the RL conversion measurement of the large-area CsPbBr₃ film in a corresponding uniform dose field at $Z = 20$ cm. Similar to the dose rate measurements, the variations in RL power with tube current and voltage were measured, as shown in Fig. 4b and e, respectively. The RL power of the CsPbBr₃ film depended on the dose rate (or the number of absorbed photons). Therefore, our CsPbBr₃ film exhibits a good linear RL response to the X-ray dose rate (Fig. 4c and f) and is suitable for X-ray imaging scintillators.

3.3 Radiography and tomography of CsPbBr₃-based scintillator

A tomographic experiment of a biological sample (bamboo) was performed using high-brilliance synchrotron radiation to assess the stability of the CsPbBr₃-based scintillators. The quality of the projections collected during a 90-min interval was very high, as shown in Fig. 5a, indicating long-term radiostability. Various structures in bamboo were superimposed and could not be distinguished in tomographic images. Phase-retrieval-based projections with high contrast enable effective FBP reconstruction to reveal tiny 3D structures of the samples. The reconstructed longitudinal and transverse sections are shown in Fig. 5b

and c, respectively. The reconstructed sections show high-contrast feature structures, including subtle morphological differences between the vascular bundles and microcalcifications. The 3D visualization of bamboo was successfully reconstructed and provided multidimensional morphological information (Fig. 5d), such as the perimedullary, vascular bundles, cortex, epidermis, and subcutaneous layer, owing to the stability of the CsPbBr₃-based scintillator with an extended time and intense irradiation. The perimedullary is in the medulla with firm, tightly packed cells. The vascular bundles are distributed in the cortex between the subcutaneous layer and perimedullary gradually from inside to outside. The wall and density of the vascular bundles showed the same trend owing to fiber lignification, which developed from the outside. The fiber wall thickness increases over time. The subcutaneous layer comprises two or three layers of columnar cells with a thick cell wall, and the cells are arranged longitudinally in a columnar shape. The outermost layer is the epidermis, which has a high density and plays a protective role. The high-quality CT images (Fig. 5) also indicate that the photoluminescence performance of the film is uniform throughout the imaging region.

4 Discussion

High-quality flexible SLHP films for X-ray scintillators were synthesized using self-assembled solutions at room temperature. Compared with the traditional scintillator preparation method, this sample preparation process enabled massive film production with a large area and uniform thickness owing to low requirements of equipment and conditions. Less pollution is another crucial advantage. However, the characteristics of crack-free CsPbBr₃ film solution preparation can satisfy the need for large-area scintillators for flat-panel detectors. This CsPbBr₃ film scintillator also exhibited a very fast response ($\tau = 11.5$ ns), critical to scintillation performance in biomedical radiography. Fast response to X-rays and high light yields are suitable for the application of dynamic real-time X-ray imaging. The photostability of the CsPbBr₃ film was further measured using X-ray illuminations with different fluxes and energies under repeated cycles. The results showed consistent responses to the RL intensity and incident X-ray dose rate.

The fitting of the dose rate and RL intensity of the CsPbBr₃ film showed excellent linear relationships with increasing tube current at a fixed propagation distance because the photon flux in the field was proportional to the tube current (Fig. 4a and b). Moreover, the dose rate and RL intensity rapidly increased with decreasing distance between the testing sample and the X-ray source. The RL

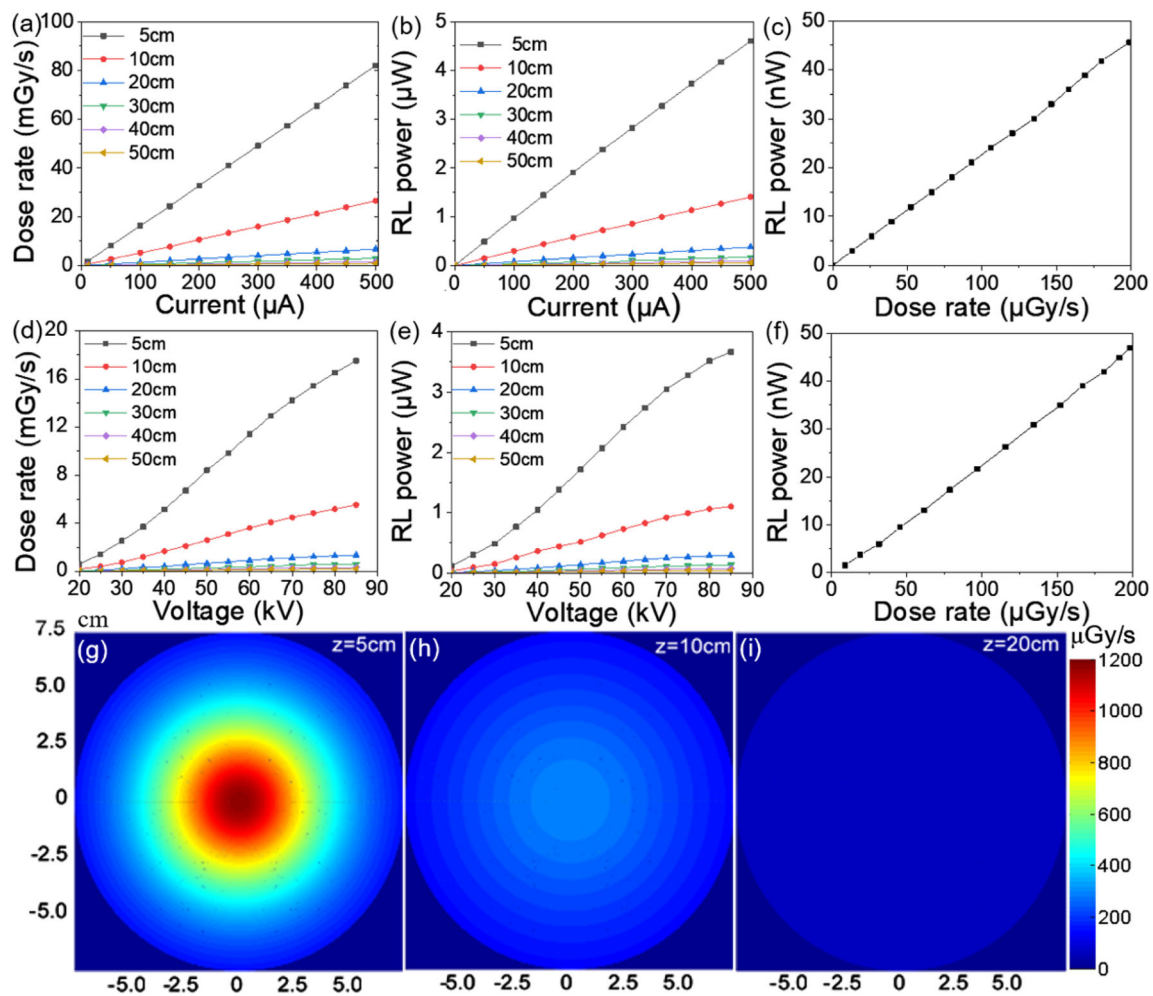


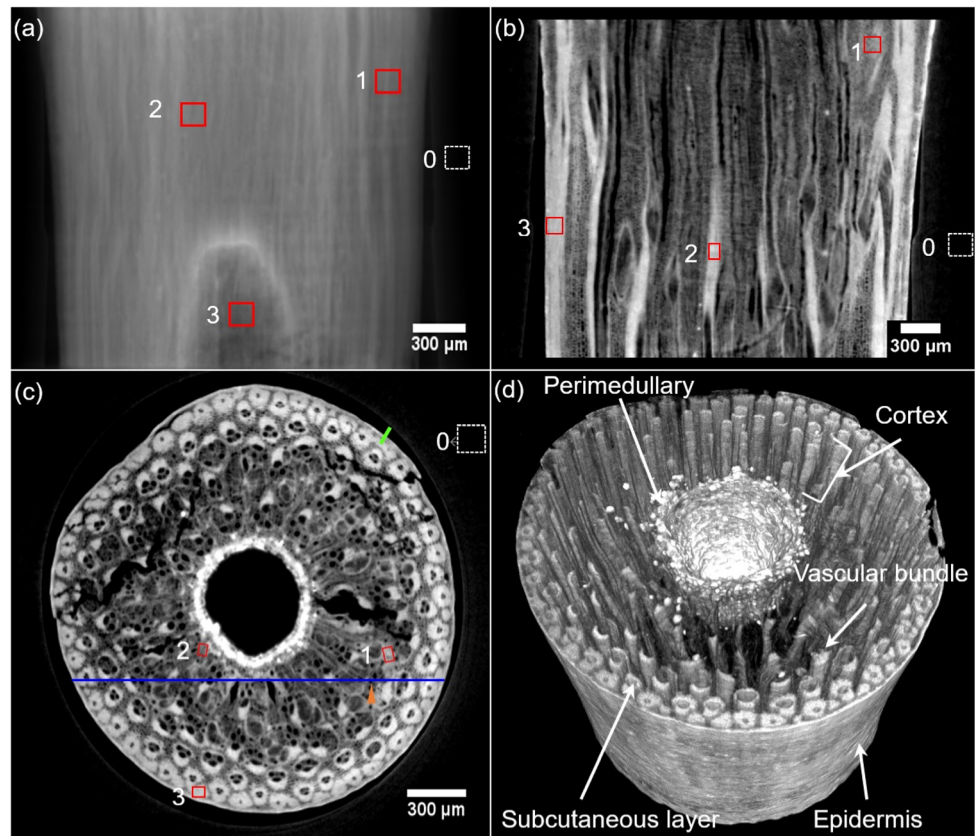
Fig. 4 (Color online) X-ray RL characterization of CsPbBr₃ scintillating film. **a** and **d** Variation in X-ray dose rate with tube current and voltage, respectively. **b** and **e** Variation in X-ray RL power with tube current and voltage, respectively. **c** and **f** Linear conversion performances of scintillating CsPbBr₃ film for tube current and voltage

dependence, respectively. **g–i** Spatial distributions of cone X-ray radiations at imaging locations $z = 5, 10,$ and 20 cm with current = $10 \mu\text{A}$ and voltage = 60 kV, suitable for radiography of samples with different sizes

of the CsPbBr₃ film responded linearly to the X-ray dose rate with a fitted slope of 0.22 (Fig. 4c). This indicates that this film can provide stable and high light yields, essential for high contrast for different X-ray attenuations. Furthermore, the photon energy characteristics of the CsPbBr₃ film were measured based on the responses of the dose rate and RL intensity to the tube voltage (Fig. 4d and e). The increase in RL intensity is not strictly proportional to the increase in the tube voltage within the range of 25–85 kV, owing to the scattering of X-rays related to photon energy. Such slight fluctuations in the photon energy responses cannot influence X-ray imaging with different photon energies for biological samples. Generally, the RL induced by X-ray photons increased with tube voltage because more high-energy X-ray photons penetrated the film and induced more quantum dot luminescence. The production of optical light in the scintillator occurs closer to the sensor

surface as the tube voltage increases, resulting in the higher light collection. The linear relationship between the dose rate and the RL intensity for the CsPbBr₃ film was calculated with a fitted slope of 0.23, based on their responses to varying tube voltages (Fig. 4f). Therefore, the measurements of the dose rate and RL intensity indicate that CsPbBr₃ films are sensitive to X-ray photon flux density, making them a potential scintillator for X-ray imaging. The radiographic image of the cable head using the CsPbBr₃-based scintillator can display their inner structures (up to $\sim 5.3 \mu\text{m}$) and characteristics with high absorption contrast, owing to the significant difference in the X-ray interactions between the metal and plastic components. Compared with the traditional scintillator with thick polycrystalline ceramics, the high SR of the CsPbBr₃-based scintillator can be attributed to the reduced degree of light scattering in the CsPbBr₃ film.

Fig. 5 Tomographic results for biological sample (bamboo) via X-ray phase-contrast microtomography with CsPbBr₃ scintillator. **a** Radiographic image. **b** Tomographic longitudinal-section image. **c** Tomographic cross-section image. **d** 3D virtual view of bamboo, indicating main botanical microstructures. ROIs 0 (dashed-line rectangle) and 1–4 (solid-line rectangle) are used for calculating CNRs. The blue line-profile plot is for measuring feature structures, and the solid green line plotted along a bamboo boundary is for measuring the LSF



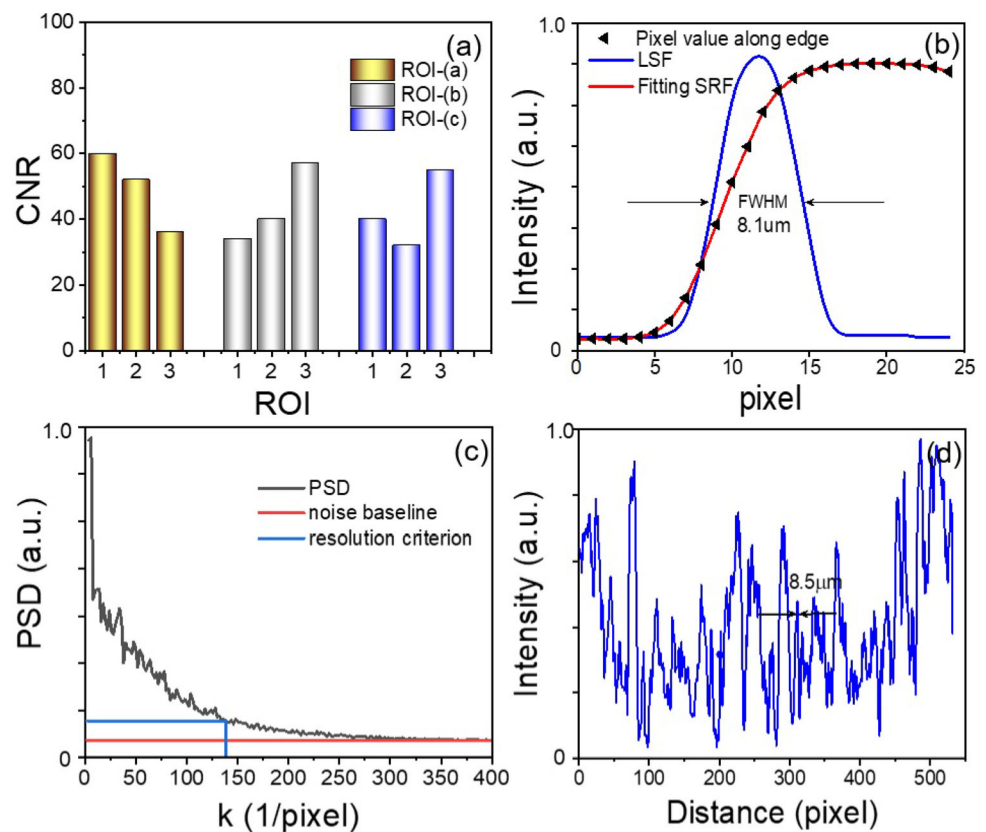
The CNR and SR determined by the scintillator stability were calculated from the ROIs manually defined in the reconstructed results to quantitatively estimate the imaging quality using our flexible CsPbBr₃ scintillator (Fig. 6a–c). The CNRs of the tomographic and radiographic images of biological samples could reach 35–60% for different density components, on average, at the 45% level (Fig. 6a). The ROIs of the subcutaneous layer or edge of vascular bundles had higher CNR values than others because of their high density and smoothness. Compared with the average CNR of 36% for the imaging of biological samples using the P43 powder (Gd₂O₂S:Tb⁺) scintillator reported in our previous study [38], a significant improvement in CNR was observed owing to the enhanced light yield of the CsPbBr₃ perovskite film. The CsPbBr₃ perovskite film can provide good structural visibility and enable image segmentation for sample feature analysis.

Image sharpness can reflect the SR of an imaging system and is essential for observing biological fine structures. It is influenced by several factors, such as the thickness and uniformity of the scintillator, effective pixel size, and source quality. An adequate thickness requires a trade-off between a high SR and a light yield efficiency, and nonuniformity results in geometric aberration and heterogeneous scattering effects. The SR estimations for our biological sample measurements were performed using the

FWHM of the LSF (from the solid green line plotted along a bamboo boundary) and PSD, reaching a minimum of 8.1 μm (Fig. 6b and c). An excellent SR can be used for analyzing fine biological sample structures. For the discrimination of a tiny structure, a blue line profile was measured (Fig. 5c), and feature size of 8.5 μm was identified (Fig. 6d). In our previous study [39], the SR of reconstructed images of biological samples measured with the P43 powder (Gd₂O₂S:Tb⁺) scintillator was reported as 8.82 μm under the same conditions as the beamline. This shows that the CsPbBr₃ perovskite film can achieve an SR level almost equal to those of current commercial scintillators. Our results demonstrate that the CsPbBr₃-based scintillator has an imaging capacity with high contrast and low noise level and is suitable for 3D nondestructive visualization of biological samples.

Because of the excellent performance evaluation of the CsPbBr₃-based scintillator, the reconstructed slices were vividly rendered for 3D visualization of the morphological features of the bamboo (Fig. 7a). Their local volumetric microstructures are shown in Fig. 7b. Various functional vascular bundles with different tissue densities can be quantitatively segmented and pseudocolored owing to the high SNR of the scintillator, which helps analyze the mechanism of plant nutrient transport systems. In addition, the morphologies of the epidermal system and

Fig. 6 (Color online) Quantitative evaluation of computed tomography with CsPbBr₃-based scintillator. **a** CNRs in Fig. 5a–c. SR analysis based on FWHM of LSF in (b) and PSD in (c). The plotted line-profile show the specific microstructural size in (d)



perimedullary tissue can be observed, and their distribution characteristics clarify the assessment of the hardness and growth of bamboos. The sparse area of vascular bundles around the perimedullary region was segmented and removed because of the low density of the nascent tissue. In particular, the histogram in the inset of Fig. 7c provides effective segmentation thresholds for the depositional distribution of inorganic salts. In addition, the volumetric extractions of age-related calcium oxalate crystal clusters (Fig. 7c) are formed by numerous calcifications, accounting for more than 95% of all calcifications and the remaining near the epidermis. Moreover, the statistical distributions of the geometrical characteristics of different functional components, including the cross-sectional area of the vascular bundle, the cluster volume of the calcium oxalate crystal, and the microcalcification ratio, were quantitatively obtained (Fig. 7d–f), which clarifies the physiological mechanisms of bamboo. Most vascular bundle cross-sectional areas were smaller than 200 μm² (Fig. 7d), indicating that the bamboo is young. The sample consists of fibrous conduits, sieve tubes, and other cells, and its main function is to transport water, inorganic salts, and nutrients. Calcifications with small volumes (215–250 μm³) accounted for 75.65% and were related to growth

time. With the continuous increase in lifespan, the cells continued to accumulate calcification, and the calcification proportion was 11.26% in this sample. This information is vital for plant growth research. Therefore, this CsPbBr₃-based scintillator can be used for hard X-ray computed tomography with good stable performance.

5 Conclusion

Our self-assembled CsPbBr₃-based film has the advantage of flexible, large-area synthesis at room temperature. It exhibited strong RL intensity in the X-ray field and linear response characteristics to radiation dose rate, making it suitable for application in high-quality X-ray scintillators. Moreover, the developed CsPbBr₃ film scintillator also exhibited high CNR (an average of 45%) and SR (a minimum of 8.1 μm) based on the good uniformity and stability of the self-assembled CsPbBr₃-based film, which exhibited the CNR advantages compared to the commercial P43 powder scintillators. Our experimental study demonstrates that the new scintillator material has potential for use in low-dose high-resolution X-ray microtomography for biomedical samples.

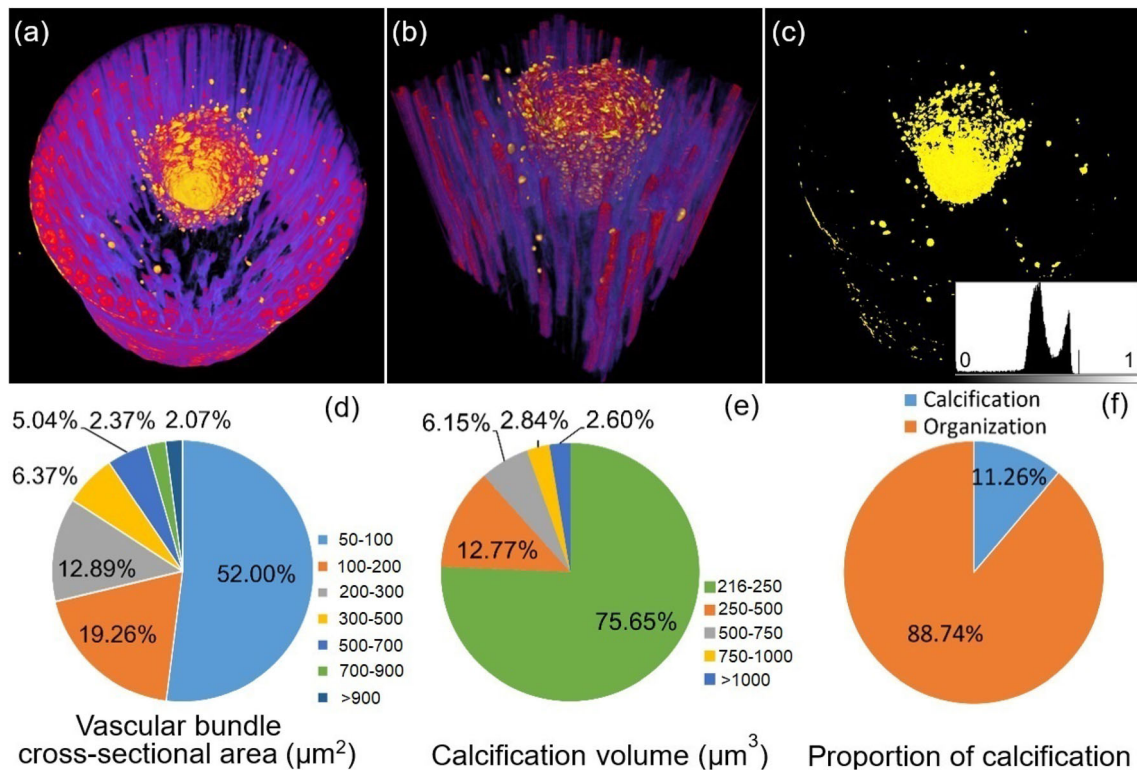


Fig. 7 (Color online) Quantitative segmentation and statistical analysis based on 3D reconstructed results obtained from CsPbBr₃ scintillator. **a–c** 3D renderings of characteristic botanic structures (inset shows the high-contrast histogram), including vascular bundles

and microcalcified clusters. **d–f** Size distributions and volume ratios of different components in bamboo tissues. The numbers represent the size and classified range in the legend

Acknowledgements We thank the staff of BL13HB (BL13W1) Beamline, X-ray Imaging and Biomedical Application, for their assistance in data collection.

Author contributions Writing and experiments were carried out by Zhi-Wei Lü and Gong-Xiang Wei. Sample preparation was done by Ning Jiang, Yun-Yan Liu, and Zhao Li. Data collection and analysis were done by Zhi-Wei Lü, Han-Qiu Wang, and Yu Guan. Design and revision of the manuscript were done by Hua Qin and Hui-Qiang Liu.

Funding This work was supported by National Natural Science Foundation of China (No. 12175127) and Natural Science Foundation of Shandong Province, China (No. ZR2020MA088).

References

- V. Cnudde, M.N. Boone, High-resolution X-ray computed tomography in geosciences: A review of the current technology and applications. *Earth-Sci. Rev.* **123**, 1–17 (2013). <https://doi.org/10.1016/j.earscirev.2013.04.003>
- M. Dierolf, A. Menzel, P. Thibault et al., Ptychographic X-ray computed tomography at the nanoscale. *Nature* **467**, 436–439 (2010). <https://doi.org/10.1038/nature09419>
- E. Maire, P.J. Withers, Quantitative X-ray tomography. *Int. Mater. Rev.* **59**, 1–43 (2013). <https://doi.org/10.1179/1743280413y.0000000023>

- S.W. Wilkins, T.E. Gureyev, D. Gao et al., Phase-contrast imaging using polychromatic hard X-rays. *Nature* **384**, 335–338 (1996). <https://doi.org/10.1038/384335a0>
- L. Vásárhelyi, Z. Kónya, Á. Kukovecz et al., Microcomputed tomography-based characterization of advanced materials: a review. *Mater. Today Adv.* **8**, 100084 (2020). <https://doi.org/10.1016/j.mtadv.2020.100084>
- M. Nikl, A. Yoshikawa, Recent R&D trends in inorganic single-crystal scintillator materials for radiation detection. *Advanced Optical Materials* **3**, 463–481 (2015). <https://doi.org/10.1002/adom.201400571>
- S. Liu, X. Feng, Z. Zhou et al., Effect of Mg²⁺ co-doping on the scintillation performance of LuAG: Ce ceramics. *Phys. Status Solidi. RRL* **8**, 105–109 (2014). <https://doi.org/10.1002/pssr.201308199>
- C. Michail, I. Valais, I. Seferis et al., Measurement of the luminescence properties of Gd₂O₂S:Pr, Ce, F powder scintillators under X-ray radiation. *Radiat. Meas.* **70**, 59–64 (2014). <https://doi.org/10.1016/j.radmeas.2014.09.008>
- M.J. Weber, Inorganic scintillators: today and tomorrow. *J. Lumin.* **100**, 35–45 (2002). [https://doi.org/10.1016/S0022-2313\(02\)00423-4](https://doi.org/10.1016/S0022-2313(02)00423-4)
- V. Thakur, A. Jain, P. Ashokkumar et al., Design and development of a plastic scintillator based whole body β/γ contamination monitoring system. *Nucl. Sci. Tech.* **32**, 47 (2021). <https://doi.org/10.1007/s41365-021-00883-1>
- H. Liu, Y. Cheng, Z. Zuo et al., Discrimination of neutrons and gamma-rays in plastic scintillator based on pulse coupled neural network. *Nucl. Sci. Tech.* **32**, 82 (2021). <https://doi.org/10.1007/s41365-021-00915-w>

12. P. Ghorbani, D. Sardari, R. Azimirad et al., Experimental study of a large plastic scintillator response with different reflective coverings based on digital pulse processing method. *J. Radioanal. Nucl. Chem.* **321**, 481–488 (2019). <https://doi.org/10.1007/s10967-019-06596-5>
13. X.L. Qian, H.Y. Sun, C. Liu et al., Simulation study on performance optimization of a prototype scintillation detector for the GRANDProto35 experiment. *Nucl. Sci. Tech.* **32**, 51 (2021). <https://doi.org/10.1007/s41365-021-00882-2>
14. A. Magi, M. Koshimizu, Y. Fujimoto et al., Development of plastic scintillators containing a phosphor with aggregation-induced emission properties. *Radiat. Meas.* **137**, 10641 (2020). <https://doi.org/10.1016/j.radmeas.2020.106401>
15. G. Ros, G. Sáez-Cano, G.A. Medina-Tanco et al., On the design of experiments based on plastic scintillators using GEANT4 simulations. *Radiat. Phys. Chem.* **153**, 140–151 (2018). <https://doi.org/10.1016/j.radphyschem.2018.09.021>
16. Z. Li, Y. Zhang, G. Cao et al., Event vertex and time reconstruction in large volume liquid scintillator detectors. *Nucl. Sci. Tech.* **32**, 49 (2021). <https://doi.org/10.1007/s41365-021-00885-z>
17. S.M. Carturan, F. Pino, C.L. Fontana et al., Temperature effects on light yield and pulse shape discrimination capability of siloxane based scintillators. *Eur. Phys. J. C* **80**, 1057 (2020). <https://doi.org/10.1140/epjc/s10052-020-08640-1>
18. N.K. Desai, P.G. Mahajan, A.S. Kumbhar et al., Nanoporous p-terphenyl-polystyrene films containing perylene; fabrication, characterization and remarkable fluorescence resonance energy transfer based blue emitting properties. *J. Mater. Sci. Mater. Electron.* **27**, 1118–1129 (2015). <https://doi.org/10.1007/s10854-015-3860-z>
19. C. Aberle, C. Buck, B. Gramlich et al., Large scale Gd-beta-diketonate based organic liquid scintillator production for antineutrino detection. *J. Instrum* **7**, P06008 (2012). <https://doi.org/10.1088/1748-0221/7/06/p06008>
20. Y. Wu, G. Ren, F. Meng et al., Effects of Bi³⁺ codoping on the optical and scintillation properties of CsI: Tl single crystals. *Phys. Status Solidi. A* **211**, 2586–2591 (2014). <https://doi.org/10.1002/psa.201431299>
21. P. Zhang, B. Jiang, Y. Jiang et al., YAG/Nd:LuAG composite laser materials prepared by the ceramization of YAG single crystals. *J. Eur. Ceram. Soc.* **38**, 1966–1971 (2018). <https://doi.org/10.1016/j.jeurceramsoc.2017.12.013>
22. H. Pan, Q. Liu, X. Chen et al., Fabrication and properties of Gd₂O₂S: Tb scintillation ceramics for the high-resolution neutron imaging. *Opt. Mater.* **105**, 109909 (2020). <https://doi.org/10.1016/j.optmat.2020.109909>
23. Y. Zhang, R. Sun, X. Ou et al., Metal halide perovskite nanosheet for X-ray high-resolution scintillation imaging screens. *ACS Nano* **13**, 2520–2525 (2019). <https://doi.org/10.1021/acsnano.8b09484>
24. Q. Chen, J. Wu, X. Ou et al., All-inorganic perovskite nanocrystal scintillators. *Nature* **561**, 88–93 (2018). <https://doi.org/10.1038/s41586-018-0451-1>
25. Y.C. Kim, K.H. Kim, D.Y. Son et al., Printable organometallic perovskite enables large-area, low-dose X-ray imaging. *Nature* **550**, 87–91 (2017). <https://doi.org/10.1038/nature24032>
26. Q.A. Akkerman, V. D'Innocenzo, S. Accornero et al., Tuning the optical properties of cesium lead halide perovskite nanocrystals by anion exchange reactions. *J. Am. Chem. Soc.* **137**, 10276–10281 (2015). <https://doi.org/10.1021/jacs.5b05602>
27. Y. Wang, X. Li, S. Sreejith et al., Photon driven transformation of cesium lead halide perovskites from few-monolayer nanoplatelets to bulk phase. *Adv. Mater.* **28**, 10637–10643 (2016). <https://doi.org/10.1002/adma.201604110>
28. W. Wei, Y. Zhang, Q. Xu et al., Monolithic integration of hybrid perovskite single crystals with heterogenous substrate for highly sensitive X-ray imaging. *Nat. Photon.* **11**, 315–321 (2017). <https://doi.org/10.1038/nphoton.2017.43>
29. J. Glodo, Y. Wang, R. Shawgo et al., New developments in scintillators for security applications. *Phys. Procedia.* **90**, 285–290 (2017). <https://doi.org/10.1016/j.phpro.2017.09.012>
30. X. Ji, H. Liu, Y. Xing et al., Quantitative evaluation on 3D fetus morphology via X-ray grating based imaging technique. *Int. J. Imaging. Syst. Technol.* **29**, 677–685 (2019). <https://doi.org/10.1002/ima.22354>
31. Y. Bekenstein, B.A. Koscher, S.W. Eaton et al., Highly luminescent colloidal nanoplates of perovskite cesium lead halide and their oriented assemblies. *J. Am. Chem. Soc.* **137**, 16008–16011 (2015). <https://doi.org/10.1021/jacs.5b11199>
32. J. Song, J. Li, X. Li et al., Quantum dot light-emitting diodes based on inorganic perovskite cesium lead halides (CsPbX₃). *Adv. Mater.* **27**, 7162–7167 (2015). <https://doi.org/10.1002/adma.201502567>
33. Q.A. Akkerman, S.G. Motti, A.R. SrimathKandada et al., Solution synthesis approach to colloidal cesium lead halide perovskite nanoplatelets with monolayer-level thickness control. *J. Am. Chem. Soc.* **138**, 1010–1016 (2016). <https://doi.org/10.1021/jacs.5b12124>
34. S. Sun, D. Yuan, Y. Xu et al., Ligand-mediated synthesis of shape-controlled cesium lead halide perovskite nanocrystals via reprecipitation process at room temperature. *ACS Nano* **10**, 3648–3657 (2016). <https://doi.org/10.1021/acsnano.5b08193>
35. X. Zhang, X. Bai, H. Wu et al., Water-assisted size and shape control of CsPbBr₃ perovskite nanocrystals. *Angew Chem. Int. Ed. Engl.* **57**, 3337–3342 (2018). <https://doi.org/10.1002/anie.201710869>
36. J. Shamsi, Z. Dang, P. Bianchini et al., Colloidal synthesis of quantum confined single crystal CsPbBr₃ nanosheets with lateral size control up to the micrometer range. *J. Am. Chem. Soc.* **138**, 7240–7243 (2016). <https://doi.org/10.1021/jacs.6b03166>
37. G. Lovric, S.F. Barre, J.C. Schittny et al., Dose optimization approach to fast X-ray microtomography of the lung alveoli. *J. Appl. Crystallogr.* **46**, 856–860 (2013). <https://doi.org/10.1107/S0021889813005591>
38. H. Liu, F. Lin, J. Lin et al., Phase-retrieval-based synchrotron X-ray micro-tomography for 3D structural characterization and quantitative analysis of agalloch eaglewood. *Wod. Sci. Technol.* **52**, 839–854 (2018). <https://doi.org/10.1007/s00226-018-1004-3>
39. H. Liu, X. Wu, T. Xiao, Optimization of reconstructed quality of hard x-ray phase microtomography. *Appl. Opt.* **54**, 5610–5618 (2015). <https://doi.org/10.1364/AO.54.005610>

Springer Nature or its licensor holds exclusive rights to this article under a publishing agreement with the author(s) or other rightsholder(s); author self-archiving of the accepted manuscript version of this article is solely governed by the terms of such publishing agreement and applicable law.